Influence of Dimensionless Temperature on Droplet Impact onto Heated Liquid Films for Subcooled Boiling Regimes

Daniel Vasconcelos*[1], André Silva[1], Jorge Barata[1]
[1]Universidade da Beira Interior, Covilhã, 6200-001, Portugal
*Corresponding author: daniel.vasconcelos.rodrigues@ubi.pt

Abstract

Heat and mass transfer mechanisms related to multiphase flows occur in several applications such as spray cooling, quenching, internal combustion engines and plasma spraying. These mechanisms have become increasingly important due to the need of achieving higher heat rate coefficients associated with phase-change processes, such as evaporation and condensation. Specifically, the phenomenon of droplet impact onto non-heated liquid films has been extensively researched, both experimentally and numerically. However, the influence of temperature on droplet impact and liquid film stability has been overlooked in the literature, which is a focal point in understanding interfacial phenomena.

The main objective of this work is to experimentally study droplet impact onto heated liquid films. Therefore, an experimental facility was designed for this purpose. A borosilicate glass surface is used to contain the liquid film. This surface is placed above an aluminium block with four embedded cartridge heaters of 250W each, heating the liquid film by conduction. Immersion type-k thermocouples are employed for liquid film temperature measurements. Liquid film evaporation rates are calculated in order to ensure the liquid film thickness prior to the droplet impact.

Water and n-decane are the fluids adopted due to their differences in thermophysical properties and saturation temperature. The impact conditions are $100 < We < 300$, $0.5 < h^* < 1.5$, and a dimensionless temperature of $\theta < 0.6$. Qualitative analysis is performed regarding crater and central jet evolution, and quantitative data regarding evaporation rate and central jet height are measured. The dimensionless temperature affects the droplet impact phenomena, creating recirculation zones near the crater and the impact surface, and affecting the crater formation. The central jet height increases with increasing values of θ for $h^* = 1.0$ and $h^* = 1.5$, whereas for $h^* = 0.5$, the measurements do not follow a similar tendency. The emerging time of the central jet is delayed for higher values of θ, meaning that future studies regarding crater evolution should be considered. The dimensionless temperature also promotes central jet breakup, as well increasing the number of secondary droplets originated from the breakup.

Keywords

Droplet Impact, Dimensionless Temperature, Heated Liquid Film, Evaporation Rate, Central Jet Breakup

Introduction

In modern times, heat transfer mechanisms and mass transfer potential occur in several applications such as spray cooling, quenching and internal combustion (IC) engines. Understanding and optimization these processes, related to phase change and heat transfer, are crucial for achieving higher heat rate coefficients. For these applications involving multiphase flows, the phenomena of droplet impact onto liquid films has been extensively researched, both experimentally and numerically, in terms of droplet impact dynamics and interfacial phenomena. However, the influence of temperature on droplet outcome, local evaporation/boiling effects, and liquid film stability has been overlooked in the literature, which is a focal point in understanding these processes [1].

Most recently, several authors have been researching droplet impact onto heated liquid films regarding fire suppression. Fan et al. [2] investigated water droplet impact onto high-temperature

peanut oil for different droplet diameters and oil temperatures. The results show that three different regimes, such as secondary jet, bubble and vapour explosion, were observed for the Weber number and oil temperature variation. These regimes are characterised by water-oil interactions, immiscible properties and saturation temperatures. Kumar et al. [3] studied the impact of a cold methanol droplet onto a hot mustard oil film for shallow and deep pool regimes. Several cavity retraction dynamics were visualised, such as normal cavity retraction and droplet pinch-off for lower oil temperatures, and vapour plume bursting and explosion for higher temperatures. Xu et al. [4] identified different impact behaviours for water droplets impacting ethanol liquid surfaces. These are divided onto crater-jet, penetration and surface bubble, and appear consecutively as the Weber number and pool temperature increase. Results suggest that the Weber number is a major factor in the maximum crown height, whereas the liquid pool temperature does not display a clear influence on this parameter. Wang et al. [5] studied similar phenomena, focusing on water droplet impact onto engine oil. Typical phenomena visualised by the authors include penetration, crater-jet, and crater-jet-secondary jet. The maximum jet height and crater volume both increase with the temperature of the oil pool and the Weber number.

These studies were primarily focused on deep liquid pool and immiscible liquids for fire suppression, meaning that the liquid film thickness was not a factor in these experiments. However, from an IC engine perspective, thin liquid films are predominant, which are phenomenologically distinct from deep pools. Therefore, the main objective of the current work is the experimental study of droplet impact onto heated thin liquid films. Qualitative analysis includes crater and central jet formation, whereas quantitative study refers to the evaporation rate and central jet height measurements.

Experimental Setup

The experimental configuration is displayed in figure 1. It is divided into five main components, which include the pumping systems, the image acquisition, the heating device, the illumination source and the impact surface. A droplet is formed at the tip of the hypodermic needle through one of the NE-1000 syringe pumps and allowed to free fall under the influence of gravity. The second syringe pump is used to counterbalance the evaporation rate to guarantee a constant liquid film thickness. This procedure will be detailed in the following section. The droplet impacts onto a stationary liquid film contained by a borosilicate glass hollow cylinder with an internal diameter of $D_c = 12\ cm$ and a thickness of $t_c = 0.5\ cm$, which is coupled to a borosilicate glass plate of $15\ cm \times 15\ cm \times 0.2\ cm$. In order to avoid leaking of the liquid film through the contact area, these are glued by an acetoxy silicone, LOCTITE® SI 5366, which is a bonding agent specifically designed for sealing and bonding up to continuous operation temperatures of $250\ ^{\circ}C$. In order to heat the liquid film, the borosilicate glass surface is placed over an aluminium block with four embedded cartridge heaters of $250\ W$ each to uniformly heat the surface by conduction and, consequently, the liquid film. The surface temperature is controlled by a heating controller which is connected to an embedded type-k thermocouple $1\ cm$ below the aluminium surface. A graphite plate of $15\ cm \times 15\ cm \times 0.4\ cm$ is positioned amidst the aluminium block and the glass surface to block reflections from the aluminium that could affect infra-red measurements in future works. In terms of image acquisition, a high-speed camera was employed for the droplet impact phenomena visualisation. A Photron FASTCAM mini UX50 with a Macro Lens Tokina AT-X M100 AF PRO D was used for the experiments at a frame rate of 4000 fps for a resolution of 1280×512 pixels. A shutter ranging from $1/16000\ s$ to $1/32768\ s$ was considered, requiring a higher shutter for lower liquid film thicknesses, and a lower shutter for higher thicknesses. The light source was provided by a LED lamp and positioned opposite to the high-speed camera, combined with a diffusion glass in between for uniform illumination.

Water and n-decane are the fluids adopted for the experiments due to their differences in thermophysical properties and saturation temperature. To measure the liquid film temperature, several type-k thermocouples were coupled to a height gauge with micrometre precision to cor-

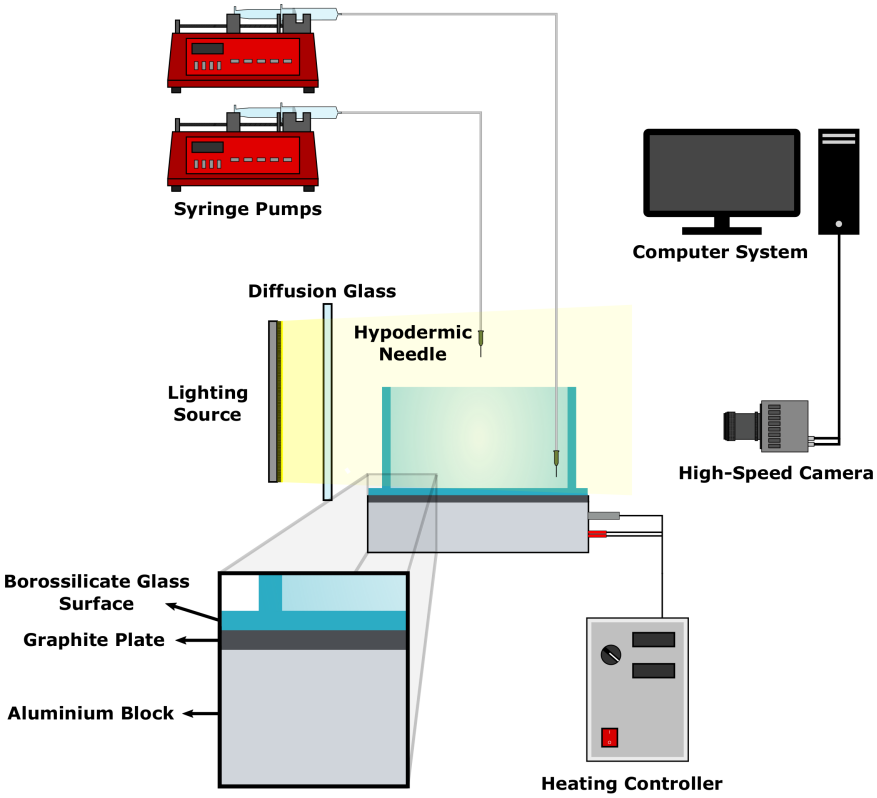

Figure 1. Schematic of the experimental setup.

rectly position the thermocouples on the liquid film. The measurements were performed at a distance of $0.1mm$ from the borosilicate glass surface.

T $[^{\circ}C]$	θ	ρ $[kg/m^3]$	μ $[Pa.s]$	σ $[mN/m]$	k $[J/\,(m.s.K)]$	C_p $[J/\,(Kg.K)]$
20	0	998.2	1.002	72.73	0.586	4183
30	0.13	995.7	0.798	71.19	0.603	4183
40	0.25	992.2	0.653	69.59	0.612	4183
50	0.38	988	0.547	67.94	0.631	4182
60	0.50	983.2	0.467	66.24	0.641	4181
70	0.63	977.8	0.404	64.48	0.650	4183

Table 1. Thermophysical properties for water at atmospheric pressure [6].

T $[^{\circ}C]$	θ	ρ $[kg/m^3]$	μ $[Pa.s]$	σ $[mN/m]$	k $[J/\,(m.s.K)]$	C_p $[J/\,(Kg.K)]$
20	0	732.1	0.929	23.89	0.133	2194
50	0.20	709.6	0.622	21.03	0.126	2261
80	0.39	686.1	0.449	18.25	0.119	2332
110	0.58	661.6	0.340	15.58	0.111	2417
140	0.78	635.7	0.264	13.01	0.102	2509
170	0.97	608.1	0.207	10.56	0.095	2626

Table 2. Thermophysical properties for n-decane at atmospheric pressure [7].

Qualitative and quantitative analysis are performed regarding crater and central jet evolution, and evaporation rate and central jet height measurements, respectively, for different temperature ranges. The quantitative data is analysed with the aid of a MATLAB algorithm based on binarization and detection of contiguous regions. Three to five droplets were analysed for each experimental condition to ensure consistency of the phenomena visualisation. The pixel size varied between $31.3\ \mu m$ and $33.4\ \mu m$.

Results and Discussion

Different impact conditions are considered for the current work, which includes three dimensionless thicknesses, $h^* = 0.5$, $h^* = 1.0$, and $h^* = 1.5$, for a range of dimensionless temperatures. Prior to droplet impact, the variation of the liquid film thickness due to evaporation must be quantified to guarantee a constant film thickness throughout the experimental study. Figure 2 displays the water and n-decane evaporation rates for different liquid film temperatures. The results are presented in mm/min due to the existence of a liquid surface whose thickness varies over time. To measure the evaporation rate, a precision scale with a $0.01g$ measurement precision is used to weigh the liquid film for extended periods of time. Relative to this work, the evaporation rate is represented by $\dot{h} = dh/dt$. The maximum relative error for the evaporation rate measurements is 1.34% for water and 1.2% for n-decane. As previously mentioned, the liquid film temperatures were measured by several type-k thermocouples coupled to a height gauge. The maximum relative error associated with the temperature measurements is 3.12% for water and 0.43% for n-decane. Due to the lower saturation temperature of water $(T_{sat} = 99.8°C)$ in comparison with n-decane $(T_{sat} = 174.1°C)$, the water evaporation rate is higher for similar temperature ranges. To guarantee a constant liquid film thickness, a second syringe pump with a pumping rate equal to the evaporation rate of the fluid is used to add liquid onto the borosilicate glass surface. The pumping occurs close to the boundaries to ensure that the temperature fields in the impact region are not affected by the liquid addition.

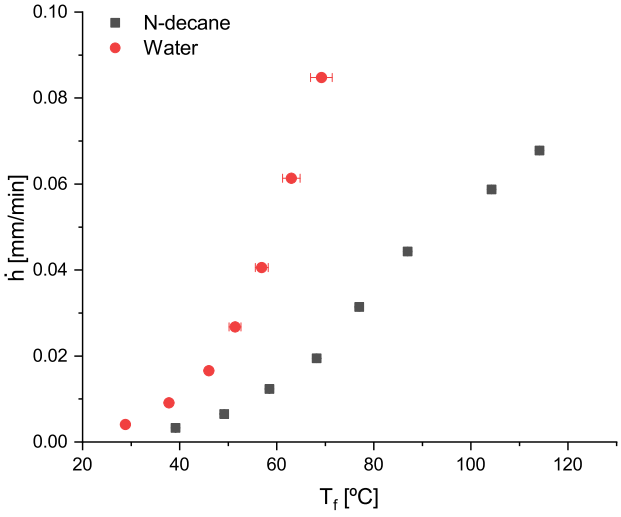

Figure 2. Evaporation rate of water and n-decane for different liquid film temperatures.

The dimensionless temperature, $\theta = (T_f - T_{air}) / (T_{sat} - T_{air})$, correlates the saturation temperature of the fluid, T_{sat}, the temperature of the liquid film, T_f, and the temperature of the surrounding air, T_{air}. For water, the dimensionless temperature range was $\theta = 0$, $\theta = 0.22$, $\theta = 0.39$ and $\theta = 0.62$. For n-decane, similar conditions were tested $(\theta = 0$, $\theta = 0.19$, $\theta = 0.37$, $\theta = 0.61)$. The Weber and Reynolds numbers were kept constant for each fluid, and calculated based on the thermophysical properties of the impinging droplet at room temperature. Therefore, the Weber and Reynolds numbers are $We = 121$ and $Re = 4869$, and $We = 261$ and $Re = 3718$ for

water and n-decane, respectively.
Figures 3a and 3b display the influence of dimensionless temperature on the crater formation of water and n-decane, respectively. The impact craters were delimited with smooth lines through binarization for improved shape visualisation. It is possible to identify for both fluids that $\theta > 0$ promotes the formation of recirculation zones. These are originated near the impact surface and the crater due to the temperature differences between the droplet and the liquid film. An increase in θ leads to the intensification of this phenomenon. In terms of crater formation, its shape is also affected for different values of θ. For water, the crater curvature near the impact surface is influenced, displaying higher local curvature for $\theta > 0$. For n-decane, the crater shifts from an oblate ($\theta = 0$ and $\theta = 0.19$) to a conical shape ($\theta = 0.37$ and $\theta = 0.61$). The curvature differences between these fluids may be associated with thermophysical properties. For $0 < \theta < 0.6$, the water and n-decane viscosity decreases with temperature, approximately 40% and 63%, respectively. The surface tension presents a similar tendency, decreasing approximately 11% for water and 35% for n-decane. Density is the thermophysical property less influenced by the temperature, decreasing 2.1% for water and 9.6% for n-decane. In terms of fluid comparison, surface tension is the thermophysical property that differs the most between the fluids, in which the surface tension variation of the n-decane is three times higher than water. This could be a major factor in comprehending how the local curvatures are affected and the influence on the subsequent impact phenomena, requiring further studies.

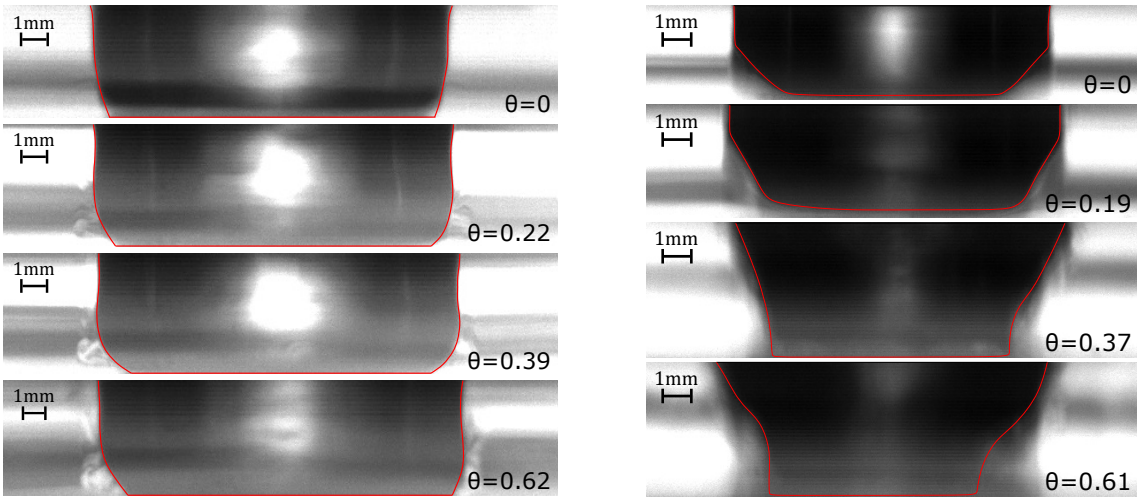

Figure 3. Crater visualisation as a function of temperature for different conditions: a) Water, $h^* = 1.0$, $\tau = 6.69$; b) N-decane, $h^* = 1.5$, $\tau = 12.03$.

Once the expanding crater reaches a maximum diameter, the following retraction may lead either to the final stages of the impact, such as coalescence for water, or to the creation of a central jet with possible breakup for n-decane. Figure 4 exhibits the central jet formation for n-decane at $\theta = 0.6$ and $h^* = 1.5$. Initially, at $\tau = 29.9$, the central jet is developing, increasing in height due to the previous crater retraction. This jet growth may lead to breakup, forming secondary droplets and reducing the jet height significantly. This can be visualised at $\tau = 33.7$, as a secondary droplet is detached from the ascending jet. The breakup phenomenon is displayed in more detail in the final two frames, for $\tau = 43.8$ and $\tau = 44.3$. For this later stage of the impact, the central jet height is decreasing until it merges with the liquid film. It is possible to observe a thin ligament at the upper region of the central jet ($\tau = 43.8$), which will rupture shortly into secondary atomization and a reduction in the central jet height ($\tau = 44.3$).
Figure 5 shows the measurements of the ratio of the central jet height to the droplet diameter, $H^*_{jet} = H_{jet}/D_0$, as a function of dimensionless time for $0 < \theta < 0.6$. The results are only displayed for n-decane due to the coalescence outcome observed for the water droplet impact (promoted by a low Weber number) and, therefore, no central jet was formed at later stages of

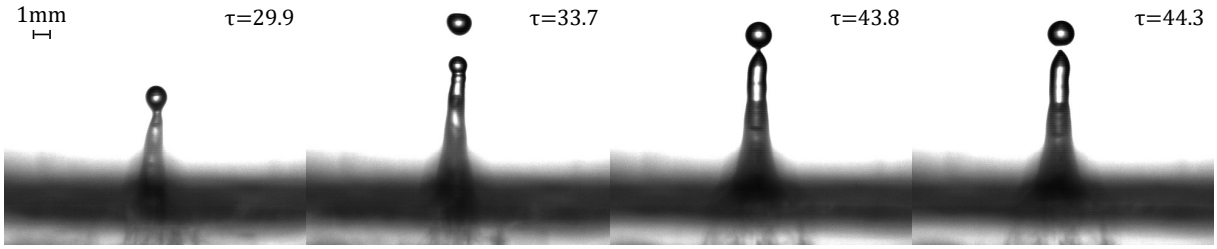

Figure 4. Central jet and breakup visualisation of the n-decane droplet impact for $h^* = 1.5$ and $\theta = 0.6$.

the impact.

For the lower thickness, $h^* = 0.5$, the results presented in figure 5a do not exhibit a clear trend for the temperature variation. The maximum jet height ranges from $H^*_{jet} = 1.11$ to $H^*_{jet} = 1.32$, showing an increase between $\theta = 0$ and $\theta = 0.2$, and $\theta = 0.4$ and $\theta = 0.6$, however exhibiting a height decrease between $\theta = 0.2$ and $\theta = 0.4$. No central jet breakup is visualised for $h^* = 0.5$, as the curves follow a continuous path, starting from the emerging central jet, reaching a maximum height, and then followed by a gradual decrease until the central jet collapses with the liquid film. As mentioned previously, the maximum height does not exhibit a clear tendency for $h^* = 0.5$. However, the emerging jet time differs with θ. For lower values of θ, such as $\theta = 0$ and $\theta = 0.2$, the emerging jet occurs for earlier stages of impact $(\tau \approx 25)$. For $\theta = 0.4$ and $\theta = 0.6$, these achieve its maximum height for later stages, meaning that the emerging jets occur for later stages $(\tau \approx 30)$.

For $h^* = 1$, in comparison with the previous case, the central jet height measurements display higher values due to the increased liquid film thickness. The results displayed in figure 5b indicate that an increase in θ leads to higher central jets, ranging from $H^* = 1.78$ for $\theta = 0$ up to $H^* = 2.98$ for $\theta = 0.6$. For $\theta \leq 0.4$, the experimental measurements show a smooth curve for all the stages of the impact. However, for $\theta = 0.6$, central jet breakup occurs at $\tau = 46.4$, leading to the formation of one secondary droplet and a sudden jet height decrease from $H^* = 2.97$ to $H^* = 1.90$. The emerging jets also display a similar tendency to the lower liquid film thickness, where the emerging jet forms earlier for lower values of θ, and gradually increase for higher values. This can also be noticed due to the maximum jet height occurring at later stages of the impact.

Figure 5c, which corresponds to the thickest liquid film, $h^* = 1.5$, shows a distinct behaviour in comparison with the lower liquid film thicknesses. Central jet breakup occurs for the different temperature ranges, $0 < \theta < 0.6$, which can be identified by the lines discontinuities associated with secondary atomization. Each line discontinuity corresponds to one secondary droplet. The number of secondary droplets formed due to jet breakup is influenced by θ. For $\theta = 0$ and $\theta = 0.2$, the central jet breaks twice, once during ascent and other after reaching its maximum height. For higher temperatures, $\theta = 0.4$ and $\theta = 0.6$, the central jet breaks up to four times, twice prior to reaching its maximum height, and then two more times during its descent. The maximum jet height also increases with θ, ranging from $H^*_{jet} = 2.92$ to $H^*_{jet} = 4.33$. As previously mentioned, the central jets also demonstrate later emergence times for increasing values of θ, which follow a similar trend to the other impact conditions.

By consolidating the different experimental results, the effect of θ on the emergence times of the central jets may be associated with the crater evolution, namely the recirculation zones and the crater shape during expansion/retraction. Future studies regarding crater parameters are required to associate local phenomena, such as temperature gradients and recirculation zones, with the emergence jet times. This effect is more notorious for $h^* = 0.5$. Regarding the jet height measurements, a higher θ leads to an increase in the maximum jet height for $h^* = 1.0$ and $h^* = 1.5$, whereas for $h^* = 0.5$ the tendency is unclear. The central jet breakup is also promoted by the dimensionless temperature, displaying one secondary droplet for $h^* = 1.0$ and $\theta = 0.6$, and ranging from two to four secondary droplets between $\theta = 0$ and $\theta = 0.6$, respectively, for $h^* = 1.5$. The influence of temperature on the central jet growth can be related to the

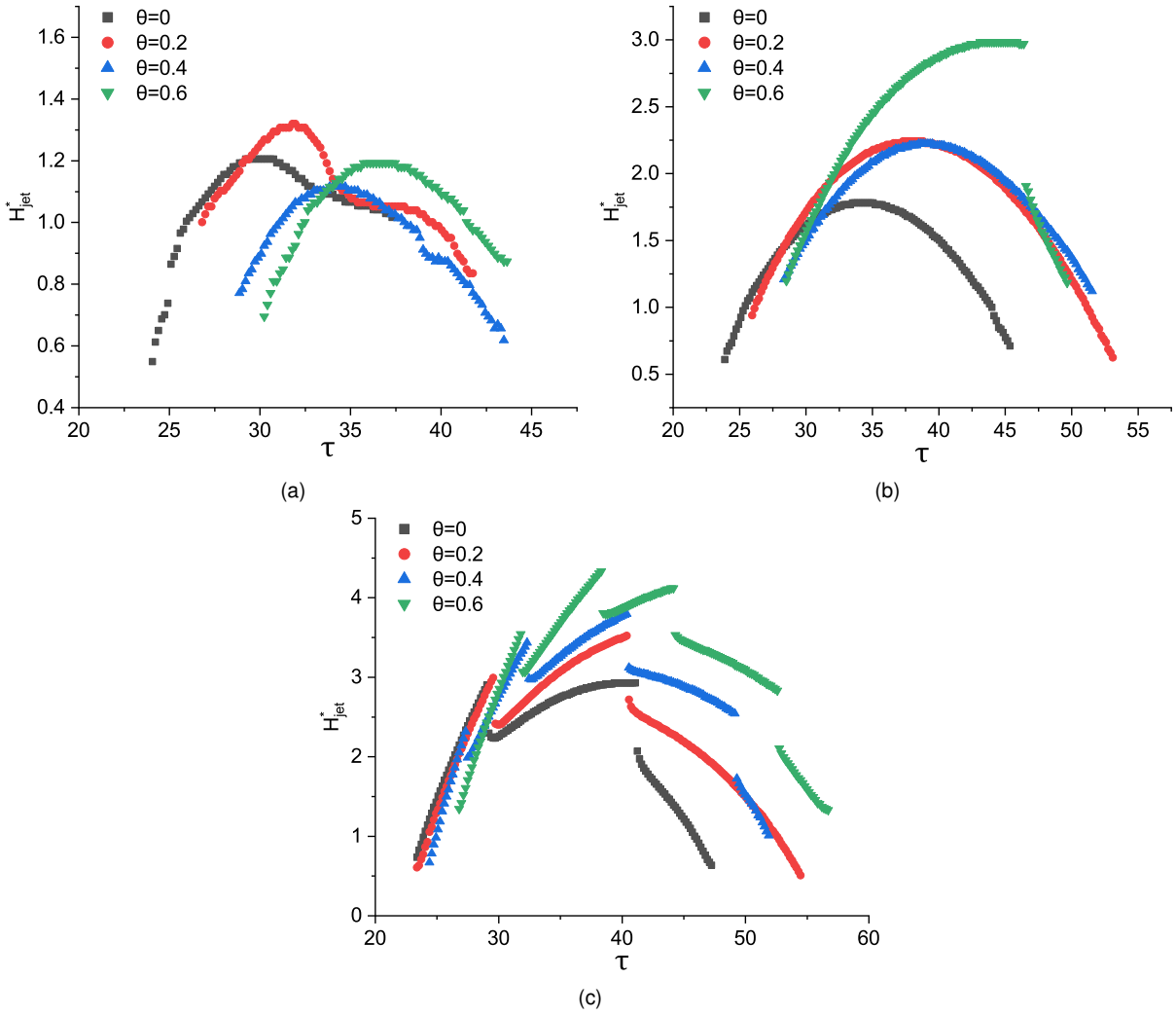

Figure 5. Central jet height measurements with n-decane for different dimensionless temperatures: a) $h^* = 0.5$ b) $h^* = 1.0$ c) $h^* = 1.5$.

differences in thermophysical properties, such as density and surface tension, as previously mentioned in the crater analysis.

Conclusions

The droplet impact onto heated thin liquid films was experimentally studied both qualitatively and quantitatively. For both fluids, it is possible to visualise the formation of recirculation zones, which are promoted by the dimensionless temperature, θ. This parameter variation also changes the crater shape and affects local curvatures. Quantitative results show that a higher θ leads to an increase in the maximum jet height for $h^* = 1.0$ and $h^* = 1.5$, whereas the tendency is unclear for lower thicknesses $(h^* = 0.5)$. The number of secondary droplets originated from the central jet breakup is also promoted for increasing values of θ. For $h^* = 1$ and $\theta = 0.6$, one secondary droplet breaks from the central, whereas for $\theta \leq 0.4$, no breakup was visualised. For $h^* = 1.5$, the secondary droplets range from two to four between $\theta = 0$ and $\theta = 0.6$. The influence of temperature on the thermophysical properties of the fluids is a factor in the phenomena overall development.

Acknowledgements

The present work was performed under the scope of Aeronautics and Astronautics Research Center (AEROG) of the Laboratório Associado em Energia, Transportes e Aeronáutica (LAETA)

activities, supported by Fundação para a Ciência e Tecnologia (FCT) through the project number UIDB/50022/2020 and by the Ph.D. scholarship with the reference SFRH BD/143307/2019.

References

[1] Liang, G., Mudawar, I., 2016, *International Journal of Heat and Mass Transfer*, 101, 577-599.
[2] Fan, X., Wang, C., Guo, F., Chen, B., Li, M., 2021, *International Journal of Thermal Sciences*, 159, pp. 106601.
[3] Kumar, R., Lokesh, Das, A. K., 2022, *Physics of Fluids*, 34(1), 012108.
[4] Xu, M., Li, C., Wu, C., Chen, X., Lu, S., 2018, *International Journal of Heat and Mass Transfer*, 116, 817-824.
[5] Wang, T., Wang, C., Rui, S., Pan, K., 2021, *Chinese Physics B*, 30(11), 116801.
[6] Dinccer, I., Zamfirescu, C., 2016, 'Drying phenomena: theory and applications', John Wiley & Sons
[7] Yaws, C. L., 2008, 'Thermophysical properties of chemicals and hydrocarbons', William Andrew